The Astrophysical Journal, 693:901–913, 2009 March 1 doi:10.1088/0004-637X/693/1/901

SUBSTRUCTURE IN THE COLD FRONT CLUSTER ABELL 3667

Matt S. Owers[1], Warrick J. Couch[2], and Paul E.J. Nulsen[3]
[1] School of Physics, University of New South Wales, Sydney, NSW 2052, Australia; mowers@phys.unsw.edu.au
[2] Center for Astrophysics and Supercomputing, Swinburne University of Technology, Hawthorn, VIC 3122, Australia
[3] Harvard Smithsonian Center for Astrophysics, 60 Garden Street, Cambridge, MA 02138, USA
Received 2008 June 30; accepted 2008 November 21; published 2009 March 3

ABSTRACT

We present evidence for the existence of significant substructure in the cold front cluster Abell 3667 based on multiobject spectroscopy taken with the 3.9 m Anglo-Australian Telescope. This paper is the second in a series analyzing the relationship between cold fronts observed in *Chandra* X-ray images and merger activity observed at optical wavelengths. We have obtained 910 galaxy redshifts in the field of Abell 3667 out to 3.5 Mpc, of which 550 are confirmed cluster members, more than doubling the number of spectroscopically confirmed members previously available and probing some 3 mag down the luminosity function. From this sample, we derive a cluster redshift of $z = 0.0553 \pm 0.0002$ and velocity dispersion of 1056 ± 38 km s^{-1} and use a number of statistical tests to search for substructure. We find significant evidence for substructure in the spatial distribution of member galaxies and also in the localized velocity distributions and, in spite of this evidence, find the global velocity distribution does not deviate significantly from a Gaussian. Using combined spatial and velocity information, we found the cluster can be separated into two major structures, with roughly equal velocity dispersions, but offset in peculiar velocity from each other by $\sim$ 500 km s^{-1}, and a number of minor substructures. We propose two scenarios which explain the radio and X-ray observations. Our data show the cold front is directly related to cluster merger activity, and also highlights the extent of optical data required to unambiguously detect the presence of substructure.

Key words: galaxies: clusters: individual (Abell 3667)

Online-only material: color figures

1. INTRODUCTION

At the pinnacle of the structure formation hierarchy, major mergers of clusters involve the largest, most massive virialized objects at the present epoch. In a major merger, up to 10^{64} erg of gravitational potential energy is dispersed among the cluster constituents, with around 15% going into the gas through shock heating, dissipation of turbulence and adiabatic compression of the intracluster medium (ICM). The majority of the energy goes into inducing peculiar motions of the galaxies and dark matter, and a small fraction into cosmic ray acceleration and magnetic field amplification. Despite some evidence pointing to rapid evolution of galaxies caused by a major merger (Caldwell & Rose 1997), the implications of mergers for galaxy evolution are not well understood, partly because of the difficulty in identifying major mergers, and also in identifying galaxies belonging to substructure. To disentangle the physics behind each of these merger driven processes in the ICM, and also to robustly identify substructure within clusters, a multiwavelength approach is required.

To this end, we have selected a sample of clusters exhibiting robust examples of cold fronts from the *Chandra* archive (Owers 2008), and this is the second in a series of papers exploring the sample by employing a multiwavelength analysis. In the first paper (Owers et al. 2009, hereafter Paper I), we present a combined X-ray and optical analysis of Abell 1201, finding multiple substructures through combination of redshift and spatial information for 321 cluster members and confirming that the cold fronts observed are a direct result of ongoing merger activity. Here, we turn our attention to Abell 3667 which is an integral component of this ongoing study, given it was one of the first cold fronts detected by *Chandra* (Vikhlinin et al. 2001a) and helped to define the cold front phenomenon. The largest spectroscopic study to date was carried out by Johnston-Hollitt et al. (2008) and based on 231 spectroscopically confirmed cluster members. They find no evidence for dynamical activity in the velocity distribution, nor any evidence of localized deviations from the global velocity structure and conclude that in order to rule out the existence of substructure, there is a need for a larger sample of cluster member redshifts. The current study uses more extensive optical data for Abell 3667, with the aim of unambiguously detecting dynamical substructure in Abell 3667 and relating it to the cold front.

At X-ray wavelengths Abell 3667 is luminous (L_X(0.4–2.4 keV) $= 5.1 \times 10^{44}$ erg s^{-1}; Ebeling et al. 1996), hot ($kT \sim 6$ keV; Knopp et al. 1996), and displays several features indicative of a major merger. The *ROSAT* X-ray observations of Knopp et al. (1996) suggested the cluster was not in dynamical equilibrium, with an overall elliptical appearance, central structure, and significant X-ray emission associated with the second D galaxy to the northwest. Perhaps the most interesting feature in the X-ray images is the surface brightness discontinuity to the southeast of the cluster center initially interpreted as a merger shock by Markevitch et al. (1999). However, the increase in both spectral and spatial resolution and sensitivity with the *Chandra* X-ray observatory provided the necessary data to conclude that the discontinuity is a cold front—a contact discontinuity at the interface of dense, cold gas cloud moving at near-sonic speed through the hotter, less dense ICM (Vikhlinin et al. 2001a). The striking sharpness of the front suggests transport processes across the front must be suppressed, and the stability of the front has led to interesting insights into the growth of hydrodynamic instabilities due to the motion of the gas cloud within the ICM (Vikhlinin et al. 2001b; Churazov & Inogamov 2004).

Abell 3667 exhibits more interesting signatures of an ongoing merger at radio wavelengths, and distinguishes itself as one of only a few clusters with two diffuse radio relics positioned symmetrically on opposing sides of the cluster periphery with their major axis perpendicular to the direction of cluster elongation (Rottgering et al. 1997). Radio relics are steep spectrum, filamentary, polarized, synchrotron sources and Rottgering et al. (1997) hypothesized that turbulence in the cluster outskirts associated with a cluster merger was responsible for reaccelerating electrons to the relativistic speeds needed to produce the observed synchrotron emission. However, Roettiger et al. (1999) were able to produce the observed properties of the radio relics by simulating a cluster merger which produced shock fronts that inject the energy required to accelerate electrons to ultra-relativistic speeds required for the synchrotron radiation (also see Hoeft & Brüggen 2007, and references therein). More indirect evidence for a merger comes in the form of a head–tail galaxy located $\sim$ 635 kpc to the northwest of the central galaxy (Rottgering et al. 1997), which according to Bliton et al. (1998) are preferentially found in dynamically active clusters.

In the optical, Abell 3667 manifests itself as a richness class 2, Bautz-Morgan I-II intermediate type cluster (Abell et al. 1989) at redshift $z = 0.055$. Girardi et al. (1998) measure a virial mass of $1.2 \times 10^{15} h^{-1}\ M_{\odot}$ and velocity dispersion 971 km s^{-1} for 154 members within 2.2 h^{-1} Mpc. Earlier work by Sodre et al. (1992) and Proust et al. (1988) measure higher dispersions (1100–1400 km s^{-1}) but with smaller samples. Despite the clear evidence of merger activity at X-ray and radio wavelengths, the existence of substructure detected at optical wavelengths remains ambiguous. Multimodality has been observed in projected galaxy density maps (Sodre et al. 1992; Proust et al. 1988), although this was not detected at high significance in the density maps of spectroscopically confirmed cluster members in Johnston-Hollitt et al. (2008). Based on the DEDICA substructure detection algorithm, Ramella et al. (2007) detect a number of substructures in Abell 3667 using spatial plus color information, whilst Joffre et al. (2000) use weak lensing to produce a projected mass map which is strongly peaked around the central D galaxy, with three other peaks at lower significance—one to the north, one coincident with the second bright D galaxy and one to the southeast of the cluster center.

In this paper, we present multiobject spectra (MOS) obtained with AAOmega at the 3.9 m Anglo-Australian Telescope (AAT), more than doubling the number of spectroscopically confirmed members of Abell 3667. In Section 2 we present the photometric catalog, selection criteria for MOS observations, and data reduction. In Section, 3 we present the method for cluster membership determination. We outline the methods used for detection of substructure in Sections 4 and 5 we discuss and summarize our analysis. Throughout the paper, we assume a standard ΛCDM cosmology where $H_0 = 70$ km s^{-1}, $\Omega_m = 0.3$, and $\Omega_{\Lambda} = 0.7$. For this cosmology and at the redshift of the cluster $1'' = 1.075$ kpc.

2. OPTICAL SAMPLE SELECTION AND OBSERVATIONS

In this section, we present the method for selection of photometric candidates for spectroscopic follow up, details of the observations conducted at the 3.9 m AAT and brief descriptions of data reduction, redshift determination, redshift accuracy, and spectroscopic completeness.

2.1. Parent Photometric Catalog

The parent photometric catalog was obtained from the Supercosmos Sky Survey (SSS) server[4] using the object catalog extraction function. Objects classified as galaxies (SSS class = 1) within a radius $R = 53'$ (3.4 Mpc) of the central dominant cluster galaxy at R.A. = $20^{\rm h}12^{\rm m}27^{\rm s}.38$, decl. = $-56^{\circ}\ 49'\ 38''.7$ were included. We further filtered the catalog such that for $R \leqslant 2$ Mpc, only objects with magnitudes $r_F \leqslant 19.0$ were included, whereas for $2 < R \leqslant 3.4$ Mpc a brighter magnitude limit of $r_F \leqslant 18.0$ was adopted. These selection criteria limited the catalog to a manageable size, given the available telescope time, while retaining the objects most likely to be cluster members. This resulted in a total of 2163 galaxies being included in our parent catalog.

To maximize the efficiency of our spectroscopic observations in terms of targeting cluster members, we ranked each galaxy in the parent catalog on the basis of its position in the color–magnitude (CM) plane (see Figure 1), as well as its projected distance from the cluster center. The position of galaxies relative to Abell 3667's red CM sequence was used as a means to weight our target selection, with the red sequence being identified using 160 spectroscopically confirmed members obtained from the NED catalog. These, and further spectroscopically confirmed members as determined in Section 3, are represented by the *green* points in Figure 1, and at magnitudes fainter than $r_F \sim 16.5$ are seen to delineate a red sequence which exhibits the usual negative slope in the CM diagram. At $r_F < 16.5$, this red sequence persists, but exhibits a positive slope, which we can only assume is due to some systematic problem in the photometry at these brighter magnitudes. This behavior, however, is not problematic for preselecting targets, since all we want to do is use the red sequence to define a likely upper red envelope, below which most cluster members reside (galaxies above are almost certainly more distant nonmembers). The *solid* straight line shown in Figure 1 (for which $b_J - r_F = 0.168 \times r_F - 1.771$) represents the red envelope that was adopted. Its position and slope were set to best include all galaxies on and bluewards of the red sequence, allowing for the systematic change in its slope and the increasing photometric scatter at fainter magnitudes. Galaxies meeting these criteria at $R \leqslant 500$ kpc from the cluster center were given the highest rank. For more remote galaxies, the rank was decreased for each additional 500 kpc step in distance from the cluster center. Galaxies lying above the red envelope were all given lower rank than those below, as well as being ranked in a similar manner by their cluster-centric distances.

For completeness, we also plot in Figure 1 objects which have been shown in Section 3 to be foreground stars (shown as the *dark blue stars*), foreground galaxies (*light blue stars*), and background galaxies (*red squares*). The small *black points* indicate objects in the field without spectra.

2.2. AAOmega Observations

Substantial new spectroscopy of Abell 3667 was obtained with the two degree field (2dF)/AAOmega multiobject spectrograph facility on the 3.9 m Anglo-Australian Telescope (AAT) during the nights of 2007 July 14–18. AAOmega is a bench-mounted dual-beam spectrograph which is fed by 400 fibers which are robotically placed within the AAT's two degree field of view at prime focus (Saunders et al. 2004; Smith et al. 2004;

[4] See http://www-wfau.roe.ac.uk/sss/

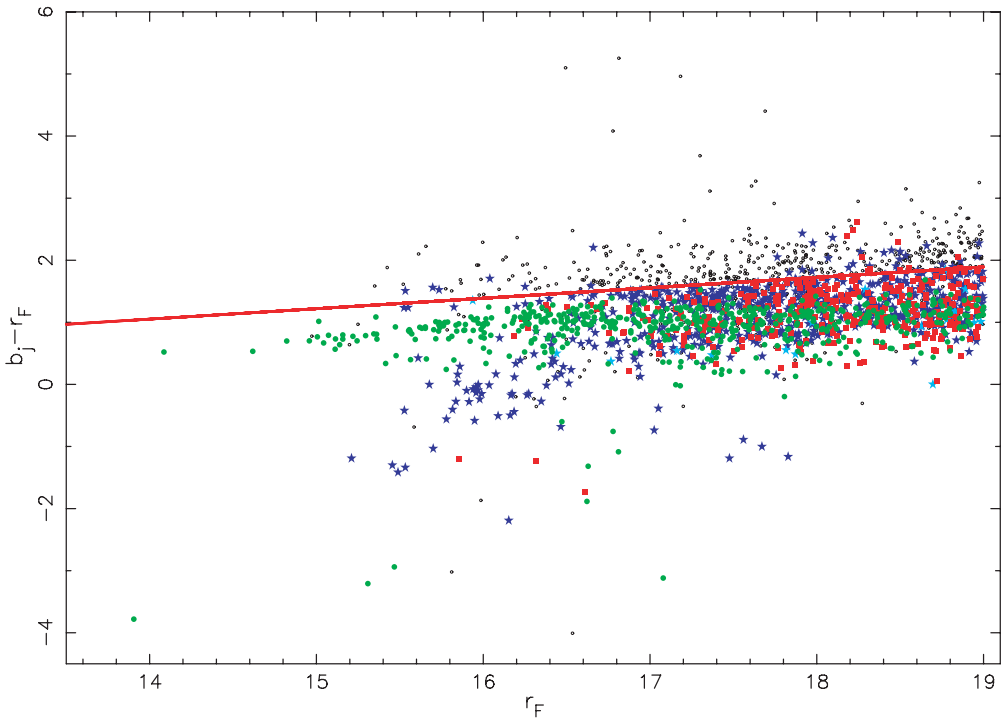

Figure 1. CM diagram for objects in the field of Abell 3667. The green points represent spectroscopically confirmed cluster members (see Section 3), the dark blue stars are foreground stars, the light blue stars are foreground galaxies, and the red squares are background galaxies. The black points are objects without spectra. The solid line shows the red envelope we adopted for separating objects which are redward of the cluster's red CM sequence and hence are likely nonmembers, from those that are on or blueward of the red sequence and hence have a high likelihood of being members.

(A color version of this figure is available in the online journal.)

Sharp et al. 2006). All observations were taken using the medium resolution ($R \simeq 1300$) 580 V (blue arm) and 385 R (red arm) gratings. In combination with the 2 arcsec diameter fibers, they deliver a spectral resolution at the detector (a 2 k×4 k 15 μm pixel E2V CCD in each arm) of 3.6 Å in the blue and 5.5 Å in the red. The wavelength range covered by the two arms is 3700–8800 Å.

The large number of galaxy targets and their highly clustered distribution on the sky, together with 30 arcsec restriction on the minimum separation between fibers, meant that six different plate configurations were required to obtain a high level of spectroscopic completeness and adequate coverage in the central regions of Abell 3667 where the cold fronts are located. The fiber allocations for each of these configurations were done automatically using the AAOmega specific *CONFIGURE* program.[5] This program uses a "simulated annealing" algorithm (Miszalski et al. 2006) to ensure the optimal allocation of fibers in terms of maximizing the number of objects observed. In doing so, it uses the rankings/weights assigned to targets (Section 2.1) to determine what priority they have in being allocated a fiber.

The use of the simulated annealing algorithm required the input catalog be reduced to no more than $\sim$ 800 objects for fiber allocation. To achieve this, the catalog was first split into the 1452 higher priority objects, on or blueward of the of the red sequence, and the 711 lower priority ones, redward of the red sequence (Section 2.1). The higher priority group were further subdivided into 830 objects with $r_F \leqslant 18$ and the 622 with $18 < r_F \leqslant 19$. Two fiber configurations were required to observe the high priority $r_F \leqslant 18$ catalog. The small number of objects in the $r_F \leqslant 18$ catalog that were not observed in these two configurations were added to the $18 < r_F \leqslant 19$ high priority catalog. Finally we constructed a catalog made up of those objects not already allocated, plus previously allocated objects with unreliable redshifts (see below) and a small number of low-priority objects. Hence in total, six configurations were observed, the majority of which targeted objects lying on or blueward of the Abell 3667's red sequence. Observing conditions were generally cloud free, but the seeing was rather poor, being in the range 2.4–4.0 arsec (FWHM). However, given the extended nature of our galaxy targets due to their relatively low redshifts, mediocre seeing did not have any serious impact on our program. The dates, exposure times, magnitudes, and conditions for the observations are summarized in Table 1.

Table 1
Summary of the AAT/AAOmega Observations for Abell 3667

Date	Object Priority	Magnitude	Frames	Seeing
2007 Jul 14	High	$r_F < 18.0$	4 × 1800 s	2.8–2.″9
2007 Jul 16	High	$r_F < 18.0$	3 × 1800 s	2.8–3.″5
2007 Jul 16	High	$r_F < 19.0$	4 × 1800 s	2.4–3.″0
2007 Jul 16,18	High	$r_F < 19.0$	2 × 1800 + 3 × 1200 s	3.″5
2007 Jul 17,18	High + Low	$r_F < 19.0$	3 × 900 + 3 × 1800 s	2.8–4″
2007 Jul 18	High + Low	$r_F < 19.0$	3 × 1200 s	3.″5

For sky subtraction, > 40 fibers per configuration were allocated to blank sky regions, selected using the "*Generate sky grid*" command in the *CONFIGURE* software and visually inspected to ensure they were free of objects. Approximately 35 known "fringing" fibers were excluded from the configuration process. Prior to each fiber configuration being observed, tungsten and arc lamp exposures were taken for flat-field and wavelength calibration, respectively. The data were fully reduced at

[5] See http://www.aao.gov.au/AAO/2df/aaomega/aaomega_software.html

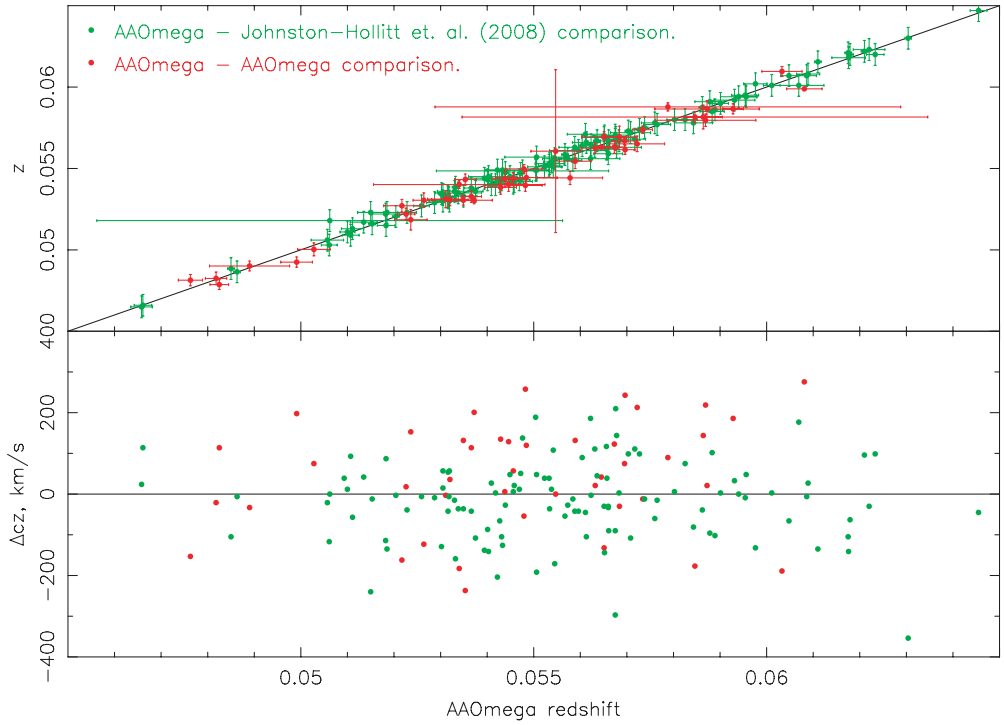

Figure 2. The top panel shows a comparison of redshift measurements for multiply observed objects where the green points show AAOmega–Johnston-Hollitt et al. (2008) redshift comparison and red points show the comparison of the AAOmega spectra with double observations. The solid black line shows the one-to-one relationship. The lower panel shows the redshift difference as a function of redshift where the color coding is as for the upper panel.

(A color version of this figure is available in the online journal.)

the telescope using the AAO 2dfdr[6] pipeline reduction system. This system extracts and produces fully flat-fielded, wavelength-calibrated, and sky-subtracted (but not flux-calibrated) spectra for each exposure frame, coadds the spectra in each exposure set, and then splices together the blue and red-arm spectra.

Redshifts were identified and measured from the reduced spectra using the runz code written by Will Sutherland for the Two Degree Field Galaxy Redshift Survey (2dFGRS; Colless et al. 2001). This program utilizes the cross-correlation method of Tonry & Davis (1979). Each spectrum was visually inspected and given a redshift quality classification, Q, ranging from 1 to 6, as described in Paper I. A Q value of 3, 4, or 5 indicates a reliable redshift was obtained (with a larger value indicating a higher quality spectrum), whereas Q values less than 3 indicate either an unreliable redshift or no redshift was obtained. A value of $Q = 6$ was used in cases where the redshift indicated the object to be a star. We obtained 1714 spectra during the run, of which 1570 yielded reliable ($Q > 2$) redshift measurements containing 910 extragalactic objects and 660 stellar objects ($Q = 6$), indicating the unreliability of the SSS star/galaxy classifications.

2.3. Redshift Measurement Uncertainties

Of the objects observed twice, 50 had two reliable ($Q > 2$) redshift measurements and so in these cases we were able to compare redshifts to assess the robustness of our measurements and determine their uncertainty. After excluding one obvious outlier where the redshift difference was $\Delta cz = 12732$ km s^{-1}, we found $\overline{\Delta cz} = 50 \pm 20$ km s^{-1} for the difference between the first and second groups of measurements. We also have 117 high-quality measurements in common with the redshift catalog of Johnston-Hollitt et al. (2008) and we found $\overline{\Delta cz} = -18 \pm 9$ km s^{-1}, again after excluding one outlier with $\Delta cz = 16134$ km s^{-1}. These redshift comparisons are encapsulated in Figure 2, noting that we only consider objects in the redshift range 0.045–0.065 (i.e., that appropriate to Abell 3667). The upper panel of Figure 2 shows that the redshift comparisons scatter about a one-to-one relationship (*solid line* with slope unity), indicating there are no redshift-dependent systematic effects. The redshift differences are shown in the lower panel. We derive an RMS redshift difference of 151 km s^{-1} for the AAOmega double observations, which implies a redshift uncertainty of 107 km s^{-1} for the sample, comparable to the RMS of the individual redshift uncertainties which is 112 km s^{-1}. An external check is given by the RMS of the differences between our AAOmega and Johnston-Hollitt et al. (2008)'s redshifts, which gives an uncertainty of 64 km s^{-1}, much lower than the quadrature sum of 148 km s^{-1} for the uncertainty above and the uncertainty of the (Johnston-Hollitt et al. 2008) sample ($\sim$ 100 km s^{-1}). We take the precision of our redshift measurements to be the more conservative value of 107 km s^{-1}.

In cases where a galaxy had multiple redshift measurements, the following policy was adopted in determining which value would be used for our analysis. If both the measurements were made with AAOmega, we adopted the redshift with the higher Q value. If the Q values were equal, then we took the redshift with the smallest measurement uncertainty (as provided by the runz program). If the second redshift measurement came from Johnston-Hollitt et al. (2008)'s catalog, we used our AAOmega redshift (for consistency). Only 25 extra redshifts were added to our catalog from the Johnston-Hollitt et al. (2008) catalog, taking our total number of redshifts to 1595.

[6] See http://www.aao.gov.au/AAO/2df/aaomega/aaomega.html

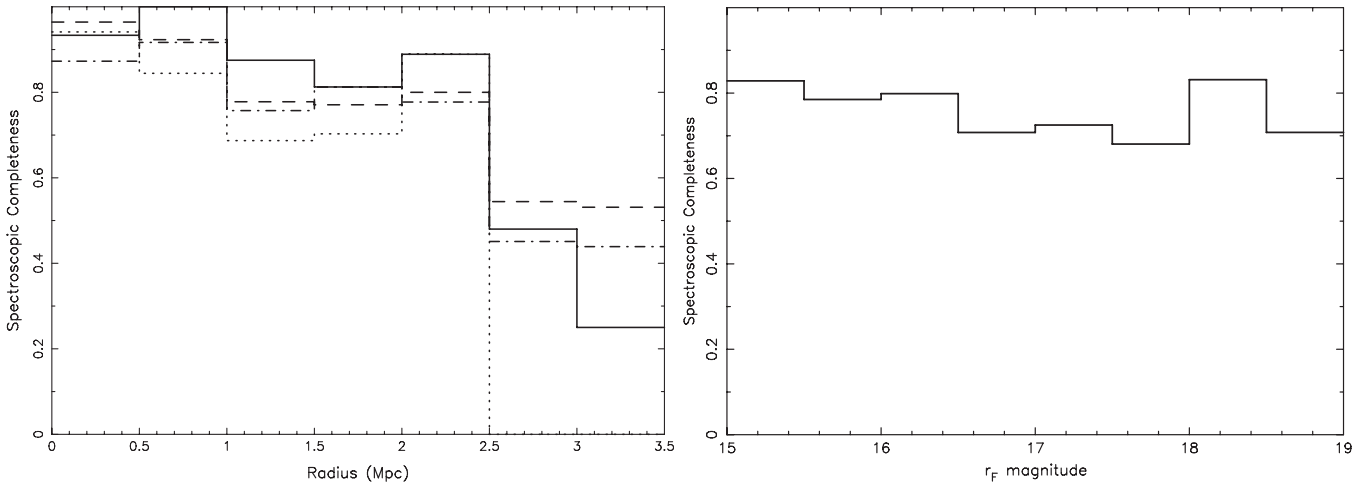

Figure 3. Left: spectroscopic completeness as a function of cluster-centric radius, for different magnitude ranges: $r_F < 16$ (solid line), $16 \leqslant r_F < 17$ (dashed line), $17 \leqslant r_F < 18$ (dot-dashed line), and $18 \leqslant r_F < 19$ (dotted line). Right: spectroscopic completeness as a function of r_F magnitude.

2.4. Redshift Completeness

The completeness of our redshift measurements was determined by calculating the fraction of galaxies in the parent photometric catalog for which reliable redshifts were obtained. In the left panel of Figure 3 we plot the completeness as a function of cluster-centric radius for the magnitude ranges $r_F < 16$, $16 \leqslant r_F < 17$, $17 \leqslant r_F < 18$, and $18 \leqslant r_F < 19$. It shows that we have achieved excellent completeness within a cluster-centric radius of 2.5 Mpc. We also plot the completeness as a function of r_F magnitude in right-hand panel of Figure 3 which demonstrates a high level of completeness across all magnitude bins. The cluster is very well sampled at magnitudes brighter than $r_F = 19$ for all radii less than 2.5 Mpc. If we assume the cluster $M^*_{r_F} = -20.84$ (Eke et al. 2004) and neglect K-correction and galactic extinction terms, we probe ~ 3 mags down the luminosity function.

3. CLUSTER MEMBER SELECTION

The major driver of this study is the detection of substructure using a sample of spectroscopically confirmed cluster members. To achieve this, it is imperative that the cluster member catalog be free of line-of-sight interlopers which may produce false substructure. Thus, a robust selection procedure is required, and we have proceeded in much the same manner as described in Paper I. Briefly, initial rejection of foreground and background objects was performed by sorting objects in redshift space, determining the velocity gap between neighboring galaxies (here velocity is defined as cz) and identifying the cluster (via the method of De Propris et al. 2002) as the peak in redshift space that is separated from foreground and background galaxies by a gap greater than some specified value. Here we use 1100 km s^{-1}, which is the velocity dispersion measured by Johnston-Hollitt et al. (2008). The redshift distribution of galaxies within the Abell 3667 field is shown in Figure 4, where Abell 3667 stands out clearly from foreground and background objects.

The membership was further refined using the "shifting gapper" method of Fadda et al. (1996) which is described in detail in Paper I. Briefly, the data are binned radially such that each bin contains 50 or more objects and interlopers are rejected in each radial bin based on gaps in the peculiar velocity distribution. Figure 5 shows the results of applying the shifting gapper method, where it is clear that a number of foreground galaxies are rejected with this refined procedure, while a number of background galaxies very close in redshift space at radii greater than 2.5 Mpc are also rejected.

Our final cluster sample contains 550 members within a cluster-centric radius of ~ 3.5 Mpc, more than doubling the number of spectroscopically confirmed cluster members previously known. Using this expanded sample, we apply the robust biweight scale and locations estimators described in Beers et al. (1990) to determine a cluster velocity dispersion, $\sigma_v = 1056 \pm 38$ km s^{-1}, and mean a redshift, $z_{\cos} = 0.0553 \pm 0.0002$ where the quoted errors are 1σ values and were determined using the jackknife resampling technique. Presented in Figure 6 are the integral and differential profiles of the location ($\mu(R)$) and scale ($\sigma(R)$) estimators. The differential profiles are determined using the radial bins from the shifting gapper analysis. The integral profiles are obtained through sorting the members by cluster-centric radius and measuring $\mu(R)$ and $\sigma(R)$ within the projected radius of each galaxy, beginning with the tenth galaxy from the center. The integrated $\sigma(R)$ becomes relatively constant outside $R = 2$ Mpc, indicating that the cluster velocity dispersion measured at this radius is free from the effects of velocity anisotropy, and is representative of the cluster's gravitational potential. The differential $\sigma(R)$ is a declining function of radius, and is significantly lower in the outskirts. The differential $\mu(R)$ measurements are noisy, but are generally consistent, within the errors, with the value measured for the whole cluster.

4. SUBSTRUCTURE DETECTION

In this section, we search for substructure using the velocity distribution, the distribution of galaxies on the sky and a combination of spatial plus velocity information. These various statistical methods have differing sensitivities to the variety of substructure that can occur in clusters (Pinkney et al. 1996; Girardi & Biviano 2002). Using a range of tests improves our chances of detecting any substructure that is present.

4.1. Quantifying the Gaussianity of the Velocity Distribution

Dynamically relaxed clusters are expected to have line-of-sight velocity distributions which are very close to Gaussian. Departures from Gaussianity in cluster velocity distributions can signify a number of different physical phenomena, e.g., highly radial orbits, interloper contamination, circular orbits and, most

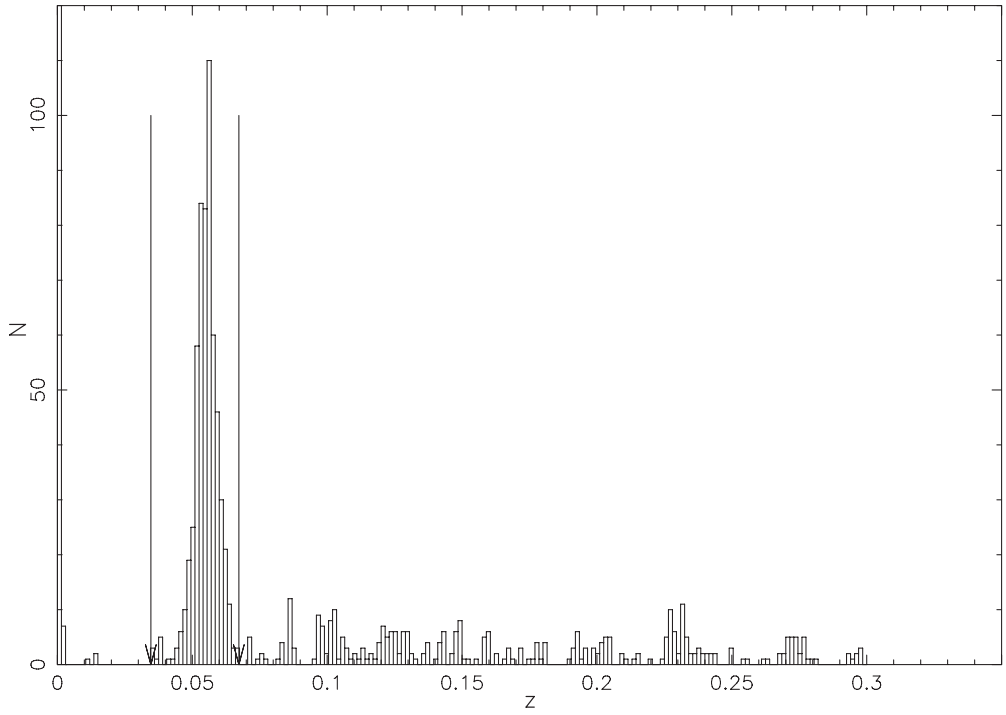

Figure 4. Redshift distribution for all robust measurements in the Abell 3667 field. Abell 3667 clearly stands out against the projected background and foreground objects. The arrows indicate the separation of the cluster based on gaps in the velocity distribution of $cz = 1100$ km s^{-1} (see the text). The bin at $z = 0$ contains some 660 stellar objects.

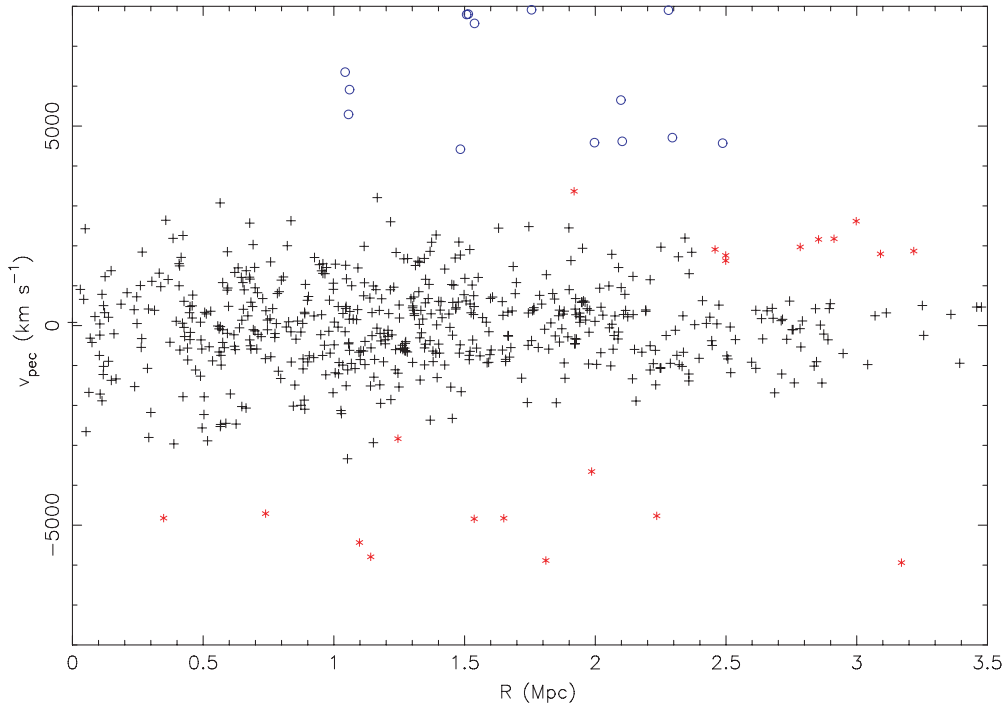

Figure 5. Refinement of cluster membership using the shifting gapper method (see the text for details). The black crosses are cluster members, red asterisks indicate objects that are rejected as interlopers and the blue circles indicate objects rejected prior to the shift gapper refinement.

(A color version of this figure is available in the online journal.)

commonly, substructure within the cluster. It must be noted, however, that nondetection of departures from Gaussianity is not necessarily evidence of a relaxed system (Pinkney et al. 1996; see also Paper I).

Our initial test for departures from Gaussianity involves the use of the Kolmogorov–Smirnov (K-S) statistic (Press et al. 1992) which measures the largest absolute departure between the cumulative probability distribution of a data sample and a theoretical distribution describing the data (here, a Gaussian) and determines the significance of the difference by calculating the likelihood that the data are drawn from a parent distribution which is Gaussian, taking into account the sample size. The

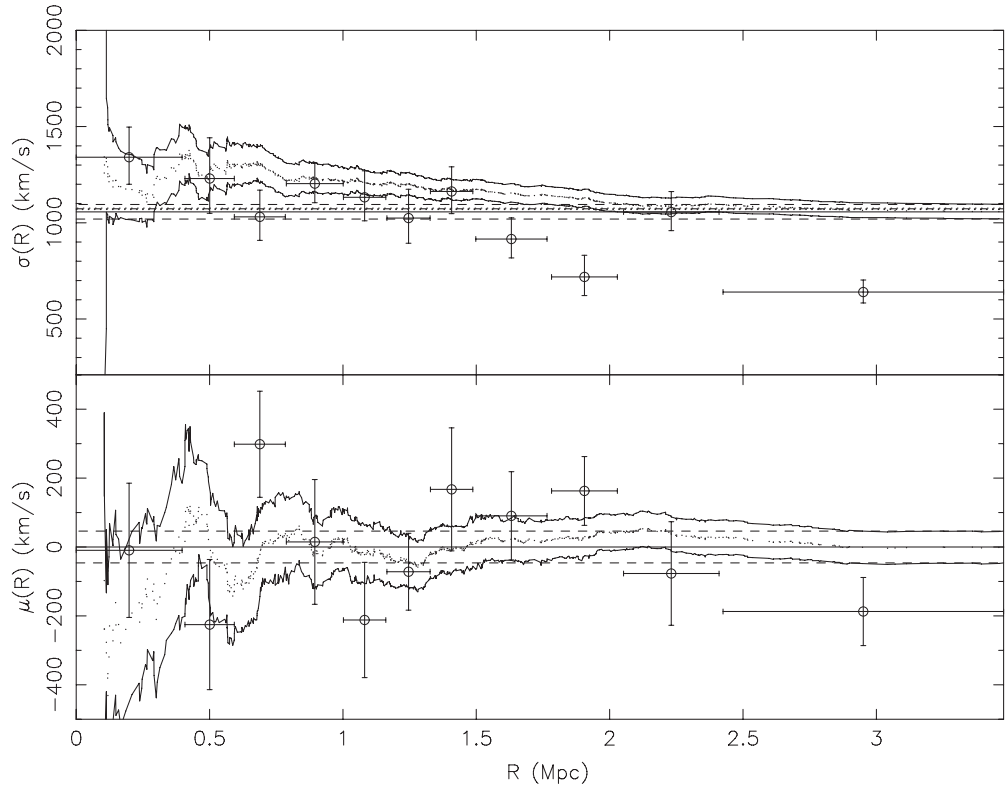

Figure 6. The top panel shows the integral (points and solid 1σ confidence limits) and differential (circles with 1σ error bars) $\sigma(R)$ measurements. Also plotted are the values measured considering all members (solid line with dashed 1σ limits), and the value obtained by assuming the same specific energy in the gas and galaxies and using the gas temperature to determine the expected velocity dispersion (dot-dashed line with dotted 90% confidence limits). The bottom panel shows the corresponding $\mu(R)$ measurements.

K-S test reveals no evidence for non-Gaussianity at the 50% level.

The disadvantages of the K-S test are its lack of sensitivity in the tails of a distribution (it is most sensitive in the vicinity of the median), its spurious results in the presence of interlopers and also its failure to quantify the way in which a distribution may differ from Gaussianity, which is clearly important in determining the physical driver of the departure from Gaussianity. Thus, we used the method first applied to galaxy cluster velocity distributions by Zabludoff et al. (1993) where the distribution is approximated by a series of three Gauss–Hermite functions: the coefficient of the zeroth-order term, h_0, multiplies a best-fitting Gaussian, the third-order term, coefficient h_3, describes asymmetric deviations from Gaussianity (similar to skewness), and the fourth-order term, coefficient h_4, describes symmetric deviations (similar to kurtosis). It has the advantage of being insensitive to outliers in the tails of the distribution (compared to the Gaussian skewness and kurtosis measurements). For Abell 3667, the third- and fourth-order terms had values of $h_3 = 0.009$ and $h_4 = 0.047$.

To determine the significance of the results, we generated 10,000 Monte Carlo realizations of Gaussians with $N = 550$ and mean and dispersion equal to the best-fitting value derived for our data, and determined the number of times our observed values occurred in the simulations. Values of $|h_3| \geqslant 0.009$ occur in 77% of the realizations, so we conclude the observed h_3 term is not significantly different from zero. Values of $|h_4| \geqslant 0.047$ occur only 10% of the time, thus we conclude the observed h_4 term is mildly significant. The positive value of the h_4 term means that the velocity distribution has slightly longer tails and is more peaked than the best-fitting Gaussian, suggestive of either radial orbits or substructure. In Figure 7 we plot the binned velocity distribution, with both a Gaussian (with a mean of zero and a standard deviation of 1056 km s^{-1}) and the Gauss–Hermite reconstruction curves overlaid.

We searched for possible segregation in the velocity distribution using weighted gaps (Beers et al. 1990), where the velocities are sorted in increasing order and the ith velocity gap is given by $g_i = v_{i+1} - v_i$. The weight for the ith gap is $w_i = i(N - i)$ and the weighted gap is defined as $\sqrt{w_i g_i}$. The weighted gaps are normalized through dividing by the mid-mean (MM) of the ordered weighted gap distribution given by

$$MM = 2/N \sum_{i=N/4}^{3N/4} \sqrt{w_i g_i}, \quad (1)$$

where $N = 550$. Normalized weighted gaps which have values larger than 2.5 occur 1.4% of the time when selecting gaps at random from a Gaussian distribution (Wainer & Schacht 1978), thus eight such gaps are expected for Abell 3667. In fact we find four such gaps, shown as arrows in Figure 7 where the positions of each peculiar velocity in the sample is plotted in a strip density plot. We conclude that the weighted gap analysis does not provide significant evidence for segregations in the velocity distribution of Abell 3667.

4.2. 2D Galaxy Distribution

While the tests for Gaussianity are useful for detecting mergers occurring along our line of sight, where the velocity distribution is significantly perturbed, they can be ineffective in the case of a merger occurring near the plane of the sky (Pinkney

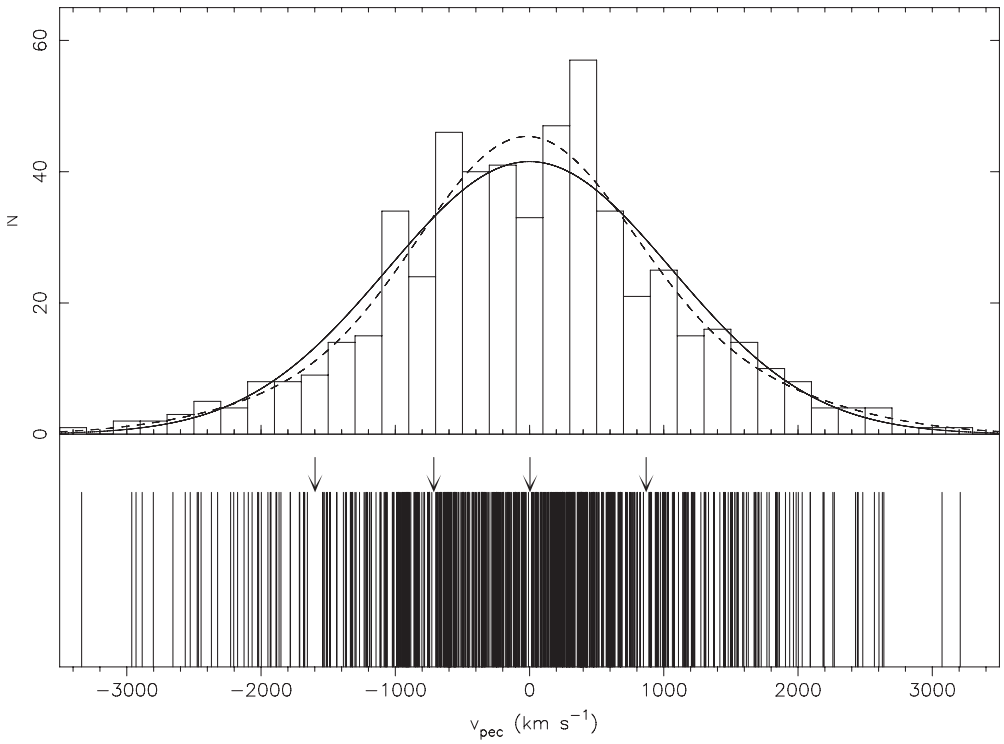

Figure 7. Top panel: peculiar velocity histogram with bins of width 200 km s^{-1}. The solid curve is a Gaussian with a mean of zero and standard deviation of 1056 km s^{-1} and the dashed curve shows the Gauss–Hermite reconstruction of the distribution. Bottom panel: a strip density plot where the arrows indicate the positions of weighted gaps with normalized values greater than 2.5 (see the text).

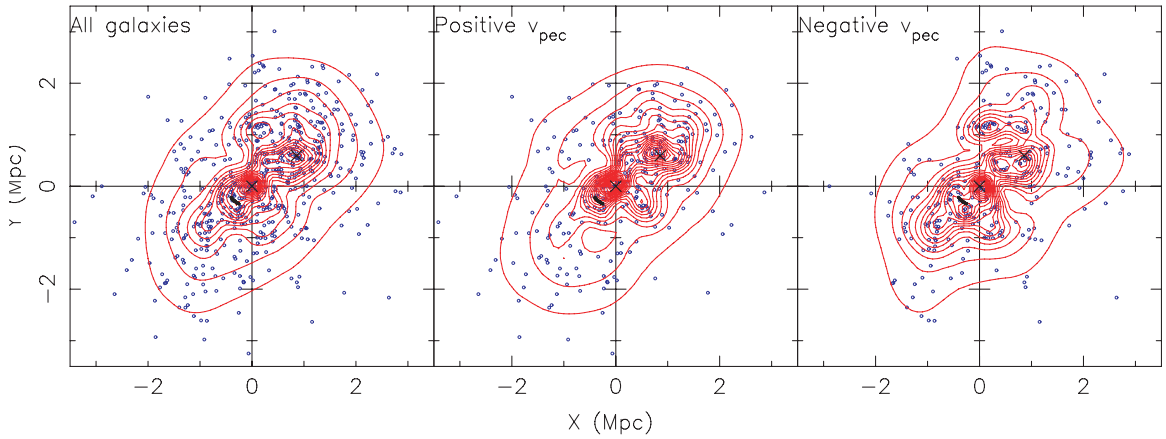

Figure 8. The leftmost panel shows the spatial distribution for the entire cluster member population with smoothed contours (see the text) drawn at 10 gals Mpc^{-2} intervals. The positive and negative velocity maps are shown in the middle and rightmost panels, respectively. The contour levels are drawn at intervals of 5 gals Mpc^{-2}. In each panel, black crosses are drawn at the positions of the two dominant cluster galaxies, and the black arc in the southeast quadrant marks the position of the cold front.

(A color version of this figure is available in the online journal.)

et al. 1996, and Paper I). In these cases, projected galaxy density maps are useful tools for searching for evidence of substructure, but are contaminated by background or foreground interlopers projected along the line of sight when redshift information is not available.

Given the presence of significant substructure apparent in the projected galaxy density maps of Proust et al. (1988) and Sodre et al. (1992), and the nondetection in of significant substructure in the maps of spectroscopically confirmed cluster members in Johnston-Hollitt et al. (2008), we use our much larger sample to produce a galaxy density map to search for signs of substructure. We plot the distribution of all galaxies in the sample, along with the associated surface density contours in the left-hand panel in Figure 8. The contours were generated by smoothing the distribution with a variable-width Gaussian, where σ varies from 140 kpc in the center to 500 kpc in the outskirts. We find similar results to Proust et al. (1988) and Sodre et al. (1992), finding Abell 3667's galaxy surface density distribution is clearly bimodal, with a high surface density core at the center and also a high-density region offset by $\sim$ 1 Mpc to the northwest which is coincident with the second dominant cluster galaxy. There are two other clear peaks in the surface density, one $\sim$ 1.2 Mpc to the southeast and one $\sim$ 1.1 Mpc just west of due north.

As a first-order test for correlation between multipeaked surface density distribution and the velocity distribution, we

split the catalog into positive and negative peculiar velocities and plot the spatial distributions. The two segregations are shown in the *middle* and *right-hand* panels of Figure 8, along with the associated galaxy surface density contours, generated using the same Gaussian smoothing described above. The most notable features upon comparing the positive and negative maps are; the southeast and northeast peaks, which are clearly more significant in the negative peculiar velocity map and the northwest peak appears in both the positive and negative maps, although it is more significant in the positive velocity map and slightly offset in the negative velocity map.

4.3. 3D Tests for Substructure

In the previous section, we searched for spatial/velocity correlations by crudely splitting the catalog into positive and negative velocity samples. In this section, we combine both velocity and spatial information to test for substructure in a more refined manner. In general it has been found that tests simultaneously employing both spatial and velocity information are most successful at detecting substructures (Pinkney et al. 1996). Here, we incorporate the k-statistic, hereafter κ_s, which was first used in the analysis of substructure within Coma by Colless & Dunn (1996). The κ_s tests for departures between local and global kinematics by determining the probability that the local velocity distribution differs from the global one. In brief, the evaluation of κ_s is performed as follows: the nearest $n = \sqrt{N}$ neighbors in projected radius from each galaxy in the sample are selected, where N is the number of cluster members. The velocity distribution of the n neighbors is compared to the velocity distribution of the remaining $N - n$ galaxies using the K-S D-statistic and the likelihood of finding a D-statistic larger than the observed D-statistic is determined. Hence, low likelihoods give an indication that the local and global velocity distributions are significantly different. The negative log of the likelihoods are summed to give an overall measure of the substructure present within the cluster. The significance of the substructure is determined by repeating the above analysis for 10,000 Monte Carlo realizations, where any correlation between the spatial and velocity distributions due to substructure within the cluster is erased by randomly shuffling the peculiar velocities in the sample, whilst maintaining spatial information. For Abell 3667, we measured an overall κ_s of 422. In contrast, the κ_s distribution produced in our Monte Carlo realizations is well modeled by a log–normal distribution with a mean of $\mu(\ln \kappa_s) = 5.44$ and standard deviation $\sigma(\ln \kappa_s) = 0.15$, indicating our result is significant at the 3.96σ level, and a value as large as 422 was not obtained in any realization.

Pinkney et al. (1996) showed that strong radial gradients in the cluster velocity dispersion profiles can produce high false positive detection rates for 3D substructure tests. With this in mind, and given that Figure 6 shows a significant gradient in the $\sigma(R)$ profiles for Abell 3667, we remeasured κ_s within the 2 Mpc region shown in Figure 9. The observed κ_s in the smaller region is 312, and a value of this order is obtained in only 12 of our 10,000 Monte Carlo realizations which produce a mean of $\mu(\ln \kappa_s) = 5.27$ and standard deviation $\sigma(\ln \kappa_s) = 0.17$, indicating the observed κ_s is significant at the 3.13σ level, again indicating the existence of substructure within Abell 3667 at high significance.

The most effective way to illustrate the substructure within the cluster is to present "bubble" plots, where circles with radii proportional to the negative log of the measured K-S likelihood are plotted at each cluster member position. This is shown in Figure 9, where regions of clustered large circles indicate the existence of substructure. Circles in this plot are color-coded, red for galaxies with positive $v_{\rm pec}$, and blue for galaxies with negative $v_{\rm pec}$. Also, galaxies having K-S likelihoods which occur in only 5% of the simulated cases are emboldened. The circles are plotted on top of the galaxy surface density contours, generated as described in Section 4.2.

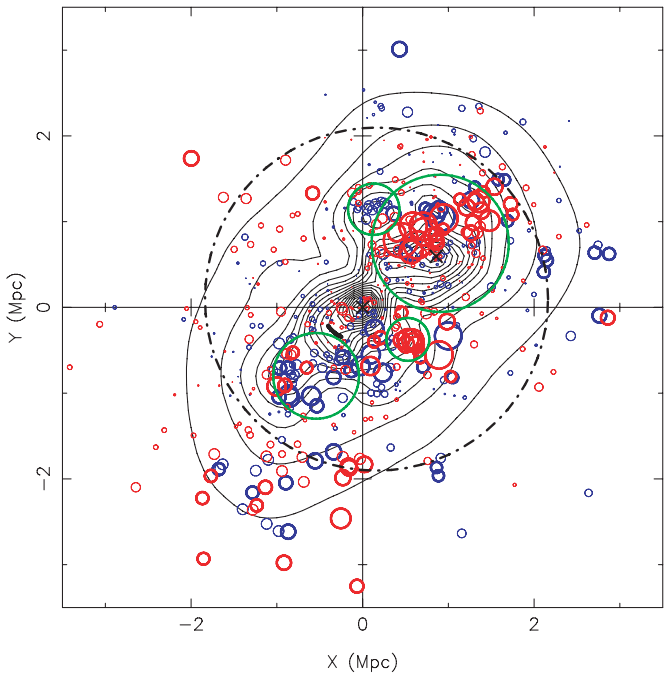

Figure 9. A "bubble" plot of Abell 3667, where the circles represent the size of the k-statistic, which provides a measure of the departure of the local velocity distribution from the global one. The circles are colored blue or red, depending on whether $v_{\rm pec}$ is negative or positive, respectively. Circles plotted with a thicker line indicate a significant departure whereby the k-statistic value occurs only in 5% of 10,000 Monte Carlo realizations. Green circles indicate regions of interest which are used as inputs to the Kaye's mixture modeling (KMM) algorithm, and the black dot-dash circle shows the region within which the KMM analysis was done. The black contours are generated as described in Section 4.2 and are plotted at intervals of 10 gals Mpc^{-2} and black crosses are drawn at the positions of the two dominant cluster galaxies, and the black arc in the southeast quadrant marks the position of the cold front.

There are a number of regions where the presence of groupings of significantly large "bubbles" indicate localized velocity structure, confirming our measure of significant substructure being present within Abell 3667. These localized regions of velocity structure are generally coincident with surface density enhancements, and, most significantly in terms of the cold front, we observe a galaxy density enhancement 700 kpc to the southeast of the front which is coincident with a clustering of large bubbles, indicating the presence of a subgroup. Interestingly, the significant enhancement in galaxy density to the northwest, coincident with the second-ranked cluster galaxy, shows little to no deviation in its local velocity distribution, despite being coincident with a peak in the projected mass maps of Joffre et al. (2000). There is, however, localized velocity structure surrounding the substructure which may be associated.

It is possible that the nondetection of localized velocity structure around the region of enhanced galaxy density to the northwest is due to the difference in the scale probed by the test compared to the physical scale of the substructure. Since the local velocity distribution is defined using a fixed number of near neighbors, rather than the near neighbors within some fixed projected radius, it is difficult to determine exactly which

Table 2
Input and Output Parameters for the KMM Algorithm. The Final Column Gives the Estimates for the Correct Allocation Rate for Each KMM Partition.

	Initial Inputs			KMM Outputs			
Group	$(\overline{x}, \overline{y}, \overline{v})$	$(\sigma_x, \sigma_y, \sigma_v)$	N_{gal}	$(\overline{x}, \overline{y}, \overline{v})$	$(\sigma_x, \sigma_y, \sigma_v)$	N_{gal}	Rate (%)
KMM1	(130, 1145, −1388)	(112, 66, 353)	10	(153, 1169, −1483)	(83, 58, 395)	9	100
KMM2	(905, 747, 408)	(368, 370, 829)	110	(879, 824, 422)	(530, 560, 1039)	164	89
KMM3	(528, −373, 1375)	(91, 89, 704)	9	(563, −415, 1457)	(64, 44, 426)	7	100
KMM4	(-542, −798, −523)	(292, 238, 489)	36	(-761, −659, −638)	(412, 326, 209)	27	73
KMM5	(0, 0, 55)	(827, 853, 1020)	284	(-144, −173, −103)	(676, 739, 1073)	242	87

Notes. The units of $\overline{x}$, $\overline{y}$, σ_x, and σ_y are kpc, and the units of $\overline{v}$ and σ_v are km s^{-1}. For $\overline{v}$ and σ_v, the median and gapper estimators are used when $N_G < 15$ and where $N_G \geqslant 15$, the biweight location and scale estimators are used.

scales are being probed at each galaxy position in Figure 9. All that is known is that where the galaxy density is high, smaller scales are probed and, conversely, where the galaxy density is low, larger scales are probed. To remedy this, and also to address the fact that substructures can have a range of different physical scales, we use a multiscale analysis. This involves remeasuring κ_s in a similar fashion to that described above, but rather than using a fixed number of n nearest neighbors to define the local velocity distributions, we use the near neighbors within a fixed projected radius, R_{NN}, of the galaxy of interest. The analysis is repeated for near neighbors within $R_{NN} = 200, 400, 800,$ and 1600 kpc and the resulting bubble plots are shown in Figure 10. For these radii, we measure κ_s values of 342 (4.15σ), 405 (3.71σ), 762 (4.62σ), and 1114 (4.04σ), respectively, where the bracketed values are the significances, measured as above from 10,000 Monte Carlo realizations. Across the four scales presented in Figure 10, all of the substructures seen in Figure 9 are reproduced and, most significantly, on scales 800 and 1600 kpc the northwest substructure appears as a region containing significant local velocity substructure.

Our concern regarding the $\sigma(R)$ gradient affecting the κ_s measurement seems warranted, given the detection of significant velocity structure >2 Mpc to the southeast in Figure 9 and the lower panels of Figure 10. This structure is not offset significantly in peculiar velocity; however its dispersion is much lower than the total cluster value and therefore it is unlikely to be a bound infalling substructure. Rather it is likely to be an artifact of the declining $\sigma(R)$ profile.

Having identified significant substructure within Abell 3667, we now use the KMM algorithm (Ashman et al. 1994) to partition the different substructures. The algorithm fits a user-specified number of Gaussians to a data set and determines the improvement of the fit over that of a single Gaussian. Here, we utilize the combination of spatial and velocity information and fit 3D Gaussians. Inspection of Figure 9 reveals four regions of interest (outlined by green circles) where there is localized velocity structure and/or there is structure in the galaxy surface density. These regions serve as an initial estimate of the number of partitions into which the KMM algorithm should divide the cluster, and we restrict our analysis to the region containing these structures defined by the black dot-dash region in Figure 9. Within the regions of interest, obvious velocity outliers are rejected, and the mean and standard deviation are measured for the spatial distributions, while the median and median absolute deviation (Beers et al. 1990) are measured for the velocity distribution. The measurements serve as initial inputs to the algorithm and, along with the outputs from the KMM algorithm, are shown in Table 2, where the final $\overline{v}$ and σ_v values are determined using the median and gapper estimators in cases where $N_G < 15$, and the biweight location and scale estimators in cases where $N_G \geqslant 15$ members, respectively.

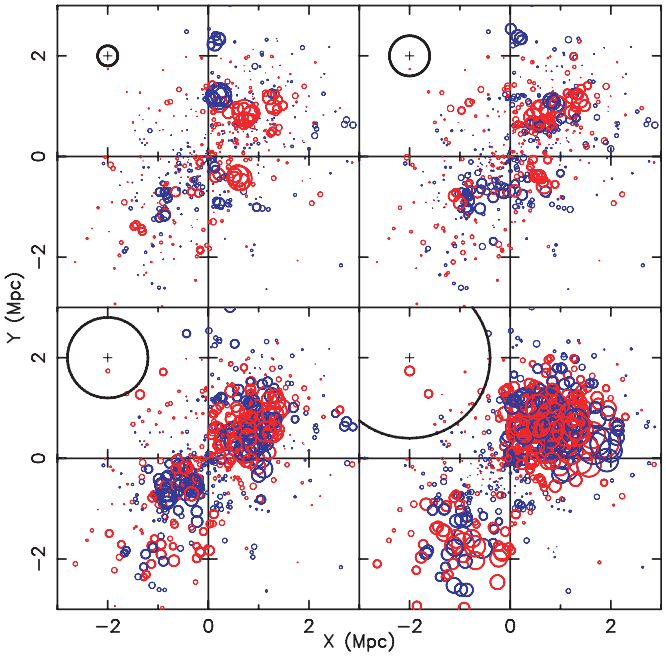

Figure 10. Multiscale bubble plots where the circle size and color is defined as in Figure 9, but rather than using the $n = \sqrt{N}$ nearest neighbors to define the local velocity distribution, we use the near neighbors within a fixed projected aperture of R_{NN}=200, 400, 800 and 1600 kpc shown in the upper left, upper right, lower left, and lower right panels, respectively. The bold black circle in the upper left of each panel has radius R_{NN}.

In Figure 11, we show the spatial distribution of the partitions, along with the associated velocity histograms for each partition. The cluster is essentially divided into northwest and southeast partitions, with the southeast one associated with the dominant cluster galaxy, and the northwest one associated with the second-ranked galaxy coincident with the second major overdensity in the galaxy surface brightness maps. The velocity dispersions of these components are very similar (1039 ± 66 km s^{-1} for KMM2 and 1073 ± 64 km s^{-1} for KMM5), but their velocities are slightly offset, with KMM2 having $\overline{v} = 422 \pm 82$ km s^{-1}, similar to the peculiar velocity of the of the second-ranked galaxy which is at 432 km s^{-1}, and KMM5 has $\overline{v} = -103 \pm 71$ km s^{-1}. There are two other minor structures (KMM1 and

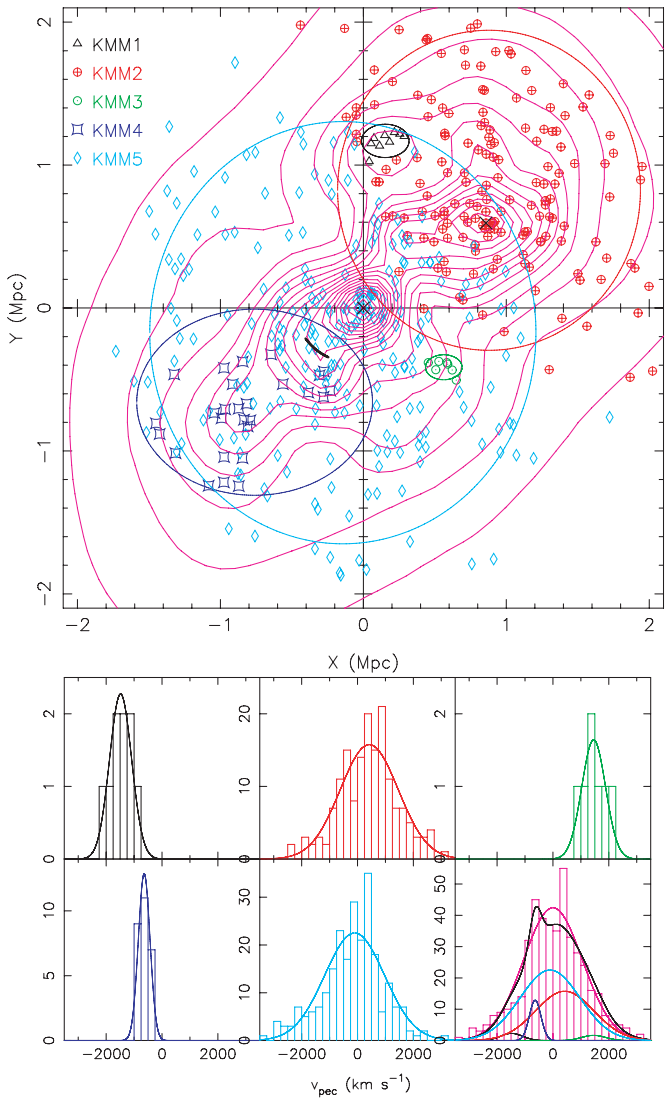

Figure 11. Upper panel: the spatial distribution of the KMM partitions. The ellipses are the 2σ boundaries for the Gaussians fitted to the spatial distributions. Galaxy contours with the same spacings as in Figure 9 are shown in pink, and the color key for the positions is given at upper left. Black crosses are drawn at the positions of the two dominant cluster galaxies, and the black arc in the southeast quadrant marks the position of the cold front. Bottom panel: the velocity histograms corresponding to the KMM partitions, color-coded to match the upper panel. At the bottom right we show the velocity distribution for all galaxies included in the KMM analysis, along with the breakdown of the Gaussian components making up the total velocity distribution. We also overplot the best-fitting single Gaussian (pink curve) for comparison.

KMM3) which appear to be small bound groups, and a low-velocity dispersion structure to the southeast (KMM4), which is associated with an overdensity in the galaxy surface density maps.

5. DISCUSSION AND CONCLUSIONS

Abell 3667 shows three signatures of a recent merger. There is significant substructure in both the spatial and localized velocity distributions of the galaxies. It has a pronounced cold front and other structure in its X-ray emitting gas (Knopp et al. 1996; Markevitch et al. 1999; Vikhlinin et al. 2001b) and it contains two radio relics (Rottgering et al. 1997). Here we consider how these structures were created.

5.1. Merger Scenario

The multiwavelength data at hand may be reconciled with a simple two-cluster merger. The structure to the northwest is clearly significant in the 2D galaxy density maps and is coincident with the second dominant cluster galaxy. The structure is also coincident with a significant mass concentration in the weak-lensing maps of Joffre et al. (2000). There is only a small offset in peculiar velocity of ~ 422 km s^{-1}, and very little difference in the velocity dispersion between the northwest substructure and the main cluster. This suggests a merger between subclusters of similar masses taking place roughly in the plane of the sky.

The direction of motion of the northwest substructure cannot be determined from the optical data alone, however it can be constrained by considering the radio and X-ray data in the literature. Regarding the radio data, the pertinent observation is the northwest radio relic described in Rottgering et al. (1997) where inference can be made regarding the direction of motion by consideration of the spectral index and brightness distribution of the relic. Rottgering et al. (1997) find that the relic brightness steepens at the northwest edge and is more diffuse to the southeast, while the spectral index is flat at the northwest edge and steepens towards the southeast. The model of Roettiger et al. (1999) explains these features as due to a shock front moving from the southeast to northwest, where the steepening of the brightness and the flatness of the spectral index at the northwest edge occur because this is where the shock acceleration of electrons is currently occurring. Since the shock moves from southeast to northwest, the electrons to the southeast no longer have a source of energy for acceleration, and the spectral index steepening is caused by the aging of the particles as the shock moves off to the northwest. It should be noted, however, that recent observations (Johnston-Hollitt 2003) have cast doubt on the existence of a flat spectral index at the northwest edge of the relic and show only a moderate spectral gradient across the source. Even without these arguments, the curvature of the radio relic is consistent with a shock propagating to the northwest. The *ROSAT* X-ray observations of Knopp et al. (1996) find significant evidence for extended X-ray emission associated with the northwest subcluster. In Figure 12, we present the Digital Sky Survey r-band image of Abell 3667 with X-ray contours from *Chandra* and *ROSAT* overlaid. The contours clearly extend to encompass the northwest substructure. The fact that the subcluster hosts an X-ray halo, together with the arguments based on the radio data, suggest that the northwest subcluster has significant mass and is moving from southeast to northwest with the majority of its motion in the plane of the sky.

In Figure 12, the cold front is seen as a compression of the X-ray contours to the southeast of the cluster center. Vikhlinin et al. (2001a) argued that the cold front is moving in a southeasterly direction at approximately the sound speed of the ICM. Based on arguments about the constant shape and the stability of the front, Vikhlinin & Markevitch (2002) predict the existence of a dark halo associated with the front, with its centroid ~ 90 kpc from the leading edge of the front. We find no evidence for any structure in the galaxy distribution in this region, and note that the weak lensing maps of Joffre et al. (2000) do not show any significant mass concentrations here either. In the two-body merger scenario, the cold front is produced when core gas is "sloshed" out of the central potential well after the core passage of KMM2, and an excellent example of this is seen in Poole et al. (2006)'s Figure 18 which shows entropy maps

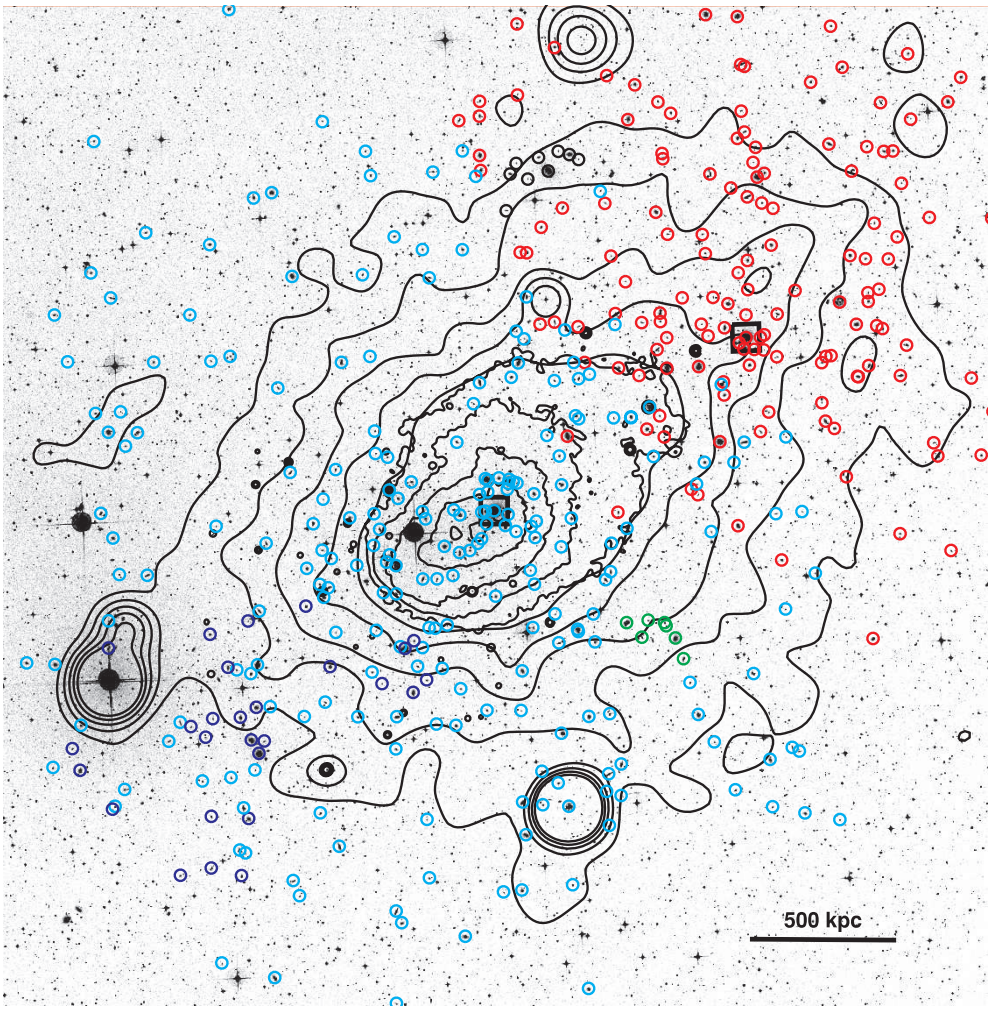

Figure 12. Digital Sky Survey r-band image of Abell 3667. Circles mark the cluster members allocated to groups using the KMM method and are color coded to match the key seen in the upper panel of Figure 11. The black contours are from archival *Chandra* (central 5 contour levels) and *ROSAT* (outer 5 contour levels) X-ray images. The cold front is visible as a compression of the X-ray contours to the southeast of the cluster center. The significant excess of emission associated with KMM2 noted by Knopp et al. (1996) is visible as an elongation of the contours toward the northwest, encompassing the KMM2 substructure. Black squares mark the positions of the two dominant cluster galaxies.

(A color version of this figure is available in the online journal.)

from the 3:1 mass ratio, offset impact parameter simulations. Interestingly, the structure that Mazzotta et al. (2002) interpret as a hydrodynamic instability is seen in these simulations and interpreted as a "plume" of cool gas ejected from the main cluster's cool core due to the subcluster's pericentric passage. These simulations also produce two shock fronts on opposite sides of the main cluster moving in opposite directions, which would account for the observed radio relics in Abell 3667. This scenario is essentially the same as that proposed in Roettiger et al. (1999), although the simulations of Poole et al. (2006) are at higher resolution and thus provide a better view of the cold front. In this scenario, KMM4 can be interpreted in two ways; in the first, KMM4 is a group either infalling from the foreground, or is a background structure that is not physically associated with the cluster, nor with any of the X-ray and radio features or the merger. The second interpretation is that KMM4 was once associated with KMM2, and was tidally stripped from the main KMM2 structure during its approach to the main cluster core and survives as a dynamically distinct substructure within the cluster.

An alternative scenario for the features seen in Abell 3667 involves a three-body merger, between KMM2, KMM4 and KMM5 where the arguments regarding KMM4 and its association with the X-ray and radio structures observed in the northwest presented above are essentially unchanged, however the cold front is the remnant core of KMM4, the centroid of which lies $\sim$ 550 kpc to the southeast of the front. A shock front driven by KMM4 is responsible for the radio relic in the southeast. In this scenario, KMM4 has traveled from the northwest and passed through the cluster core where its ICM was significantly slowed by ram pressure, while the collisionless galaxies and dark matter continued their passage towards the southeast, similar to that seen in the Bullet cluster (Markevitch et al. 2002). The mass maps of Joffre et al. (2000) indicate a significant mass concentration not quite coincident with KMM4, but offset by $\sim$300 kpc to the southwest. This lies well within the 2σ boundary seen in Figure 11, and the mass is highly likely to be associated with KMM4. The velocity dispersion of KMM4 is low and is unlikely to reflect the initial mass of the system, since the group must have been strongly affected by tidal forces and

dynamical friction during its passage through the cluster core. The mass of the group was probably not comparable to the Abell 3667 system, since its gravitational potential well was unable to stop the gas from being completely stripped from the group (see Ascasibar & Markevitch 2006, for a comparison of the effects of different mass ratios on ram pressure stripping of core gas).

5.2. Summary and Conclusions

We have presented an optical analysis of the cold front cluster Abell 3667 based on a large sample of (550) spectroscopically confirmed cluster members using data obtained on the AAT AAOmega facility. We find the cluster has a velocity dispersion of $\sigma = 1056$ km s^{-1} and redshift $z = 0.0553$. Although the velocity distribution does not differ significantly from a Gaussian, the cluster shows clear evidence of subclustering in the galaxy density plots, and also contains significant local velocity substructure according to the k-statistic. Using the KMM algorithm, the cluster can be partitioned into three main components—the main cluster (KMM5) with 242 members, $\sigma = 1073$ km s^{-1}, $\overline{v}_{\rm pec} = -103$ km s^{-1}, a northwest subcluster (KMM2) with 164 members, $\sigma = 1039$ km s^{-1}, $\overline{v}_{\rm pec} = 422$ km s^{-1}, and a southeast subgroup (KMM4) with 27 members, $\sigma = 209$ km s^{-1}, and $\overline{v}_{\rm pec} = -638$ km s^{-1}.

We confirm that Abell 3667 is a merging cluster, and the physical phenomena associated with observations at X-ray and radio wavelengths can be associated with substructure observed in the galaxy distribution, although it is apparent that detailed, combined *N*-body/hydrodynamical simulations are required to determine the plausibility of the two scenarios presented. This study highlights the need for large, deep spectroscopic samples to be used in conjunction with the full multiwavelength observations when determining the dynamical state of a cluster of galaxies. Future work will involve using the spectroscopic sample to study the galaxy properties within Abell 3667, and to correlate them with substructures within the cluster.

We have now studied in detail two clusters from our sample of "cold front" clusters selected from the *Chandra* archive, finding here, as for Abell 1201 in Paper I, that despite difficulties in determining precise merger histories, cold fronts can be directly related to cluster merger activity and thus are reliable signposts of ongoing mergers. However, it must be noted that both Abell 1201 and Abell 3667 harbor signs of merger activity (other than cold fronts) in their *Chandra* images, thus were expected to show evidences of merger activity at other wavelengths. The acid test for this claim will come from detailed observations of cold front clusters with relaxed X-ray morphologies.

We thank David Woods and Gregory Poole for useful conversations. We also thank the staff at the Anglo-Australian Observatory for their support during the observations, and in particular Matthew Colless for offering Director's Time in order for this project to be undertaken. MSO acknowledges the support of an Australian Postgraduate Award. We acknowledge the financial support of the Australian Research Council (via its Discovery Project Scheme) throughout the course of this work. PEJN was supported by NASA grant NAS8-01130.

This research has made use of the NASA/IPAC Extragalactic Database (NED) which is operated by the Jet Propulsion Laboratory, California Institute of Technology, under contract with the National Aeronautics and Space Administration.

REFERENCES

Abell, G. O., Corwin, Jr., H. G., & Olowin, R. P. 1989, ApJS, 70, 1
Ascasibar, Y., & Markevitch, M. 2006, ApJ, 650, 102
Ashman, K. M., Bird, C. M., & Zepf, S. E. 1994, AJ, 108, 2348
Beers, T. C., Flynn, K., & Gebhardt, K. 1990, AJ, 100, 32
Bliton, M., Rizza, E., Burns, J. O., Owen, F. N., & Ledlow, M. J. 1998, MNRAS, 301, 609
Caldwell, N., & Rose, J. A. 1997, AJ, 113, 492
Churazov, E., & Inogamov, N. 2004, MNRAS, 350, L52
Colless, M., & Dunn, A. M. 1996, ApJ, 458, 435
Colless, M., et al. 2001, MNRAS, 328, 1039
De Propris, R., et al. 2002, MNRAS, 329, 87
Ebeling, H., Voges, W., Bohringer, H., Edge, A. C., Huchra, J. P., & Briel, U. G. 1996, MNRAS, 281, 799
Eke, V. R., et al. 2004, MNRAS, 355, 769
Fadda, D., Girardi, M., Giuricin, G., Mardirossian, F., & Mezzetti, M. 1996, ApJ, 473, 670
Girardi, M., & Biviano, A. 2002, in Astrophysics and Space Science Library, Vol. 272, Merging Processes in Galaxy Clusters, ed. L., Feretti, I. M., Gioia, & G., Giovannini, 39–77
Girardi, M., Giuricin, G., Mardirossian, F., Mezzetti, M., & Boschin, W. 1998, ApJ, 505, 74
Hoeft, M., & Brüggen, M. 2007, MNRAS, 375, 77
Joffre, M., et al. 2000, ApJ, 534, L131
Johnston-Hollitt, M. 2003, PhD Thesis, University of Adelaide
Johnston-Hollitt, M., Hunstead, R. W., & Corbett, E. 2008, A&A, 479, 1
Knopp, G. P., Henry, J. P., & Briel, U. G. 1996, ApJ, 472, 125
Markevitch, M., Gonzalez, A. H., David, L., Vikhlinin, A., Murray, S., Forman, W., Jones, C., & Tucker, W. 2002, ApJ, 567, L27
Markevitch, M., Sarazin, C. L., & Vikhlinin, A. 1999, ApJ, 521, 526
Mazzotta, P., Fusco-Femiano, R., & Vikhlinin, A. 2002, ApJ, 569, L31
Miszalski, B., Shortridge, K., Saunders, W., Parker, Q. A., & Croom, S. M. 2006, MNRAS, 371, 1537
Owers, M. S. 2008, PhD Thesis, University of New South Wales
Owers, M. S., Nulsen, P. E. J., Couch, W. J., Markevitch, M., & Poole, G. B. 2009, ApJ, 692, 702
Pinkney, J., Roettiger, K., Burns, J. O., & Bird, C. M. 1996, ApJS, 104, 1
Poole, G. B., Fardal, M. A., Babul, A., McCarthy, I. G., Quinn, T., & Wadsley, J. 2006, MNRAS, 373, 881
Press, W. H., Teukolsky, S. A., Vetterling, W. T., & Flannery, B. P. 1992, in Numerical recipes in FORTRAN. The art of scientific computing, (2nd ed.; Cambridge: Cambridge Univ. Press)
Proust, D., Mazure, A., Sodre, L., Capelato, H., & Lund, G. 1988, A&AS, 72, 415
Ramella, M., et al. 2007, A&A, 470, 39
Roettiger, K., Burns, J. O., & Stone, J. M. 1999, ApJ, 518, 603
Rottgering, H. J. A., Wieringa, M. H., Hunstead, R. W., & Ekers, R. D. 1997, MNRAS, 290, 577
Saunders, W., et al. 2004, in SPIE Conf. Ser. 5492, Ground-based Instrumentation for Astronomy, ed. A. F. M. Moorwood & M. Iye (Bellingham, WA: SPIE), 389
Sharp, R., et al. 2006, in SPIE Ser. 6269, Ground-based and Airborne Instrumentation for Astronomy, ed. I. S. McLean & M. Iye (Bellingham, WA: SPIE) 62690G
Smith, G. A., et al. 2004, in SPIE Conf. Ser. 5492, Ground-based Instrumentation for Astronomy, ed. A. F. M. Moorwood & M. Iye (Bellingham, WA: SPIE), 410
Sodre, L. J., Capelato, H. V., Steiner, J. E., Proust, D., & Mazure, A. 1992, MNRAS, 259, 233
Tonry, J., & Davis, M. 1979, AJ, 84, 1511
Vikhlinin, A., Markevitch, M., & Murray, S. S. 2001a, ApJ, 551, 160
Vikhlinin, A., Markevitch, M., & Murray, S. S. 2001b, ApJ, 549, L47
Vikhlinin, A. A., & Markevitch, M. L. 2002, Astron. Lett., 28, 495
Wainer, H., & Schacht, S. 1978, PsychometriKa, 43, 203
Zabludoff, A. I., Franx, M., & Geller, M. J. 1993, ApJ, 419, 47